HHS Public Access

Author manuscript

Nat Nanotechnol. Author manuscript; available in PMC 2022 June 26.

Published in final edited form as:

Nat Nanotechnol. 2021 September ; 16(9): 1019–1029. doi:10.1038/s41565-021-00926-z.

Viscoelastic surface electrode arrays to interface with viscoelastic tissues

Christina M Tringides[1,2,3],

Nicolas Vachicouras[4],

Irene de Lázaro[3,5],

Hua Wang[3,5],

Alix Trouillet[4],

Bo Ri Seo[3,5],

Alberto Elosegui-Artola[3,5,6],

Florian Fallegger[4],

Yuyoung Shin[7],

Cinzia Casiraghi[7],

Kostas Kostarelos[8,9],

Stéphanie P Lacour[4],

David J Mooney[3,5,*]

[1.] Harvard Program in Biophysics, Harvard University, Cambridge, MA.

[2.] Harvard–MIT Division in Health Sciences and Technology, Massachusetts Institute of Technology, Cambridge, MA.

[3.] Wyss Institute for Biologically Inspired Engineering, Harvard University, Cambridge, MA.

[4.] Bertarelli Foundation Chair in Neuroprosthetic Technology, Laboratory for Soft Bioelectronic Interfaces, Institute of Microengineering, Institute of Bioengineering, Centre for Neuroprosthetics, École Polytechnique Fédérale de Lausanne, Geneva, Switzerland.

[5.] John A. Paulson School of Engineering and Applied Sciences, Harvard University, Cambridge, MA.

[6.] Institute for Bioengineering of Catalonia, Barcelona, Spain.

[7.] Department of Chemistry, The University of Manchester, Manchester, U.K.

[*] Corresponding author: mooneyd@seas.harvard.edu.

Author contributions:

CMT and DJM conceived the work and designed the experiments. CMT characterized all the materials and developed the conductive gels, as well as fabricated and characterized all the devices. YS fabricated the graphene flake dispersion under the supervision of CC and KK. CMT and HW developed and synthesized the PEVM. CMT and AEA made the material for the alginate gels of the *in vitro* studies. CMT and IdL carried out the cardiac *in vivo* recordings, and CMT, IdL and BRS conducted the muscular stimulation experiments. FF supplied the connectors, FF and AT performed the neural *in vivo* recordings, and AT analyzed the electrocorticography data. CMT and NV conducted all the data analysis. CMT and DJM wrote the manuscript, and CMT, DJM, and SPL discussed the results. All authors edited the manuscript.

The authors declare no competing interests.

[8] Nanomedicine Lab, National Graphene Institute and Faculty of Biology, Medicine & Health, AV Hill Building, The University of Manchester, Manchester, U.K.

[9] Catalan Institute of Nanoscience and Nanotechnology (ICN2), UAB Campus, Bellaterra Barcelona, Spain.

Abstract

Living tissues are non-linearly elastic materials that exhibit viscoelasticity and plasticity. Man-made, implantable bioelectronic arrays mainly rely on rigid or elastic encapsulation materials and stiff films of ductile metals that can be manipulated with microscopic precision to offer reliable electrical properties. Here, we engineer a surface microelectrode array that replaces the traditional encapsulation and conductive components with viscoelastic materials. Our array overcomes previous limitations in matching the stiffness and relaxation behaviour of soft biological tissues by using hydrogels as the outer layers. We introduce a hydrogel-based conductor made from an ionically conductive alginate matrix enhanced with carbon nanomaterials, which provide electrical percolation even at low loading fractions. Our combination of conducting and insulating viscoelastic materials, with top-down manufacturing, allows for the fabrication of electrode arrays compatible with standard electrophysiology platforms. Our arrays intimately conform to the convoluted surface of the heart or the brain cortex and offer promising bioengineering applications for recording and stimulation.

Implantable electrode arrays interface with tissues such as the brain and heart[1–5]. Existing devices, however, are made from materials with significantly different mechanical properties from organs. Previous studies have demonstrated that minimizing stiffness mismatch reduces damage to underlying tissues[5,6], yet currently no arrays exhibit viscous behaviour. Tissues are viscoelastic and undergo permanent deformations with applied stress[7–10]. The importance of substrate viscoelasticity on cell spreading and differentiation has been shown in cell culture[11,12], and the ability of a viscoelastic material to flow and remodel would enhance its conformability to an underlying surface.

Current microfabricated arrays contain electrodes patterned from thin films of metals[6,13]. In addition to a large mechanical mismatch with biological tissues, these metals fracture when subject to large strains. Nanomaterials, such as graphene and carbon nanotubes, have shown promise to create strong yet flexible interfaces with cells[14–17]. When dispersed in hydrogels, the nanocomposites demonstrate a lower mechanical modulus than carbon-elastomers or conductive polymers[18,19]. However, carbon-hydrogel composites are processed on centimetre-scales[20–22] with limited discussion on solvent-free methods for functional integration into microfabricated systems[23,24]. Further, the use of carbon nanomaterials is often limited to electrode coatings[25], and there is minimal adhesion between conductive hydrogels and the underlying metal tracks. Other nanomaterial systems, such as Ag-Au core-sheath nanowires[26], or Au mesh[27], have demonstrated improved tissue conformability with planar arrays, but still rely on fabrication processes not compatible with etching for precise patterning. Additionally, the electrical components are embedded in plastic or elastic encapsulation layers and hydrogels.

We propose a class of electrically conductive materials composed of an ultra-soft viscoelastic hydrogel matrix loaded with conductive carbon nanomaterials. Highly porous gels require a low amount of carbon nanomaterials to achieve percolation, while retaining a matched mechanical profile to biological tissues. Further, we fabricate fully viscoelastic arrays by surrounding the tracks with electrically insulating viscoelastic encapsulation layers (Fig. 1a). These viscoelastic arrays plastically deform to allow conformation to the complex geometry of soft tissues.

Compatibility of viscoelastic materials with biological tissues

The mechanical properties of fresh lamb brain and rat heart were first characterized as representative tissues to which the devices would be applied (Fig. 1b). Alginate hydrogels[28] were then used to match the viscoelastic properties of the tissues (Fig. 1c) (Fig. S1). Alginate hydrogels exhibit nanoscale mesh sizes,[28], and the surface tension ensures good contact with hydrophilic materials.

To study how mechanical properties impact tissue conformability, substrates of plastic (polyimide), elastic (Ecoflex), and viscoelastic (alginate) materials with comparable bending stiffness (Table S1) were placed on a mock porcine brain made of agarose (Fig. S2). The polyimide did not conform to the underlying mock brain, while the Ecoflex exhibited modest conformability. In contrast, the alginate conformed intimately around the site of placement (Fig. 1d). The alginate substrates exhibited a 2x increase in contact, as compared to the other substrates (Fig. 1e). In addition, the alginate substrates conformed to many sulci of the brain. This assay was repeated using biological tissue instead of a mock brain, yielding similar results (Fig. S3).

The ability of elastomeric and viscoelastic substrates to maintain contact over time without damaging the underlying mock tissues was subsequently compared. After placement on mock brains for two weeks, the alginate substrates had maintained their original locations, whereas the Ecoflex films had moved substantially and delaminated from the brain surface (Fig. S4). Neither substrate resulted in significant tissue compression, likely due to the low bending stiffness of the substrates. Further, the Ecoflex film geometry was unchanged, as compared to its initial shape, upon removal. However, the alginate gel had plastically deformed to match the underlying geometry of both the posterior (smaller radius of curvature) and anterior (larger radius of curvature) portions of the brain (Fig. 1f). An hour post-removal, the alginate had started to return to its initial shape (Fig. S5), and after 24 hours had recovered to its original dimensions. If a second gel was placed on top of the deformed gel, the recovery time was reduced to 3 hours. The alginate underwent over 7 cycles of conformation and relaxation with no impact to the substrate.

Finally, neural cells were seeded on gels with low and high storage moduli (soft vs stiff), and less and more viscoelastic gels (LVEG vs MVEG) (Fig. S6). Astrocytes were larger on LVEG with a higher cytoplasmic to nuclear ratio, resembling activated astrocytes on a control of tissue-culture plastic, as contrasted to cells on MVEG. The viscoelasticity appeared to play a more important role than the magnitude of the elastic modulus in the cell response (Fig. S7). Additionally, a larger fraction of astrocytes on stiff LVEG stained

positive for glial fibrillary acidic protein (GFAP+), a marker for astrocyte activation or injury, compared to the cells on either MVEG (Fig. 2a) (Fig. S8). Similar studies were performed with neurons using RGD-alginate-Matrigel interpenetrating networks (IPN)[7] of varying stiffness and viscoelasticity (Fig. S9). Primary neurons were found to extend significantly longer and a higher density of neurites on the MVEG-soft gels (Fig. 2b), and the MVEG-stiff gels exhibited the next most expansive neurite network. Repeating these studies with a coculture of primary astrocytes and primary neurons led to similar findings (Fig. 2c–d, Fig. S10–11).

A novel, ultra-soft, highly porous conductive hydrogel

Next, electrically conductive gel-based interconnects were fabricated from the soft MVEG alginate hydrogels. To enhance the limited intrinsic ionic conductivity of the alginate, both pyrene-modified graphene flakes (GF) (Supplemental Methods, Fig. S12) and carbon nanotubes (CNT) were added. These high aspect ratio carbon additives were suspended in the alginate prior to gelation (Fig. 3a), and microporous gels were fabricated by freezing gels before crosslinking to reduce the percolation threshold of conductive particles. Both nanoporous (nanoCG; no freezing before crosslinking) and microporous (microCG) conductive gels were cast in moulds, resulting in tracks that could conform to the complicated geometries of the sulci and the vasculature (Fig. 3b). The tracks were bent >180°, tied into knots without breaking, and remained in situ for multiple days without damage (Fig. S13). No swelling was observed in either the nanoCG or the microCG, and there were no changes to the electrodes nor track features over time as the conductive gels cycled between conforming to an underlying tissue and relaxing to their original shape.

Scanning electron microscopy (SEM) revealed that the inclusion of GF and CNT altered the structure of both nanoCG and microCG (Fig. 3c). In nanoCG, the surface roughness increased with more additives, and larger particle aggregates were apparent at higher quantities of carbon. GF integrated into the walls of the microCG, while the CNTs formed dense nodes throughout the microCG. When both were present in microCG, GF appeared to connect to CNT bundles, improving the probability for a percolating path. The microCG wall thickness was between 750–850 nm, which is smaller than the length of the CNT and allowed CNTs to span multiple pores. The resulting high surface area of the microCG is likely to be advantageous for interfacing with neurons.

The electrical behaviours of nanoCG and microCG were subsequently studied using 4-point probe resistance for gels that were 100 μm thick (Fig. S14), and conductivity values were compared for gels containing GF-only (Fig. 3d), CNT-only (Fig. 3e), and a combination of GF and CNT (GF+CNT) (Fig. 3f). For all cases, the microCG formulations were significantly more conductive than the nanoCG equivalents. Conductivity values greater than 10 S/m, and as high as 35 S/m, could be achieved with microCG compositions with less than 2% carbon loading (Fig. 3e, 3f). The microCG achieved the percolation threshold at ~0.9% carbon (Fig. 3g) with a residual fitting parameter of R^2=0.89. To explore the relative electrical contribution of each additive in the microCG, conductivity was plotted (colour) as a function of both GF and CNT content (Fig. 3h). The conductivity tended to increase with the amount of carbon additive, but increased more significantly with rising CNT content

(region I) than with increasing GF (region II). The conductivity increased faster and had less variability in GF+CNT gels (region III). SEM images revealed that as more carbon was added, the total porosity of the gels was not significantly affected (Fig. S15), but the distribution of pore size seemed to increase (Fig. 3i).

The various compositions were assessed to determine how added carbon impacted their mechanical properties. Rheological analysis revealed that bulk gel G' and G" were not affected in a statistically significant manner as carbon was varied from 0 to 1.4% (Fig. S16), and nanoindentation analysis of the surface mechanical properties also indicated that neither G' (Fig. 3j) nor G" (Fig. 3k) were statistically altered in the microCG as 0 to 2% carbon was added. These measurements had a wide standard deviation, and the nanoindenter tip could have been in contact with the wall or strut of the gel, a more porous area, or a region that could have been more/less rich with carbon additives. The range presented is more similar to the mechanics of heterogeneous tissues than other reported conductive composites, and the conductive components are in contact with the underlying tissue at the electrode sites only. Further, the conductive gels had no detrimental impact on the viability of exposed astrocytes (Fig. S17).

Fabrication of a viscoelastic encapsulation layer

A process to fabricate a viscoelastic encapsulation layer was next developed. As the encapsulation layer must electrically insulate each electrical track, and the ionically crosslinked alginate gels themselves do not provide electrical insulation, a thin (15 μm) layer of an insulating physically entangled viscoelastic material (PEVM) was covalently attached to a thicker (100 μm), alginate-based tough gel (TG[29]) with similar viscoelasticity as the alginate-only gels (Fig. S18), such that the TG portions were the outermost layers and in direct contact with the tissue (Fig. 4a). The insulation layer is based on a previously reported self-healing polydimethylsiloxane (PDMS[30]), which was then physically entangled with amine-terminated PDMS to provide surface-exposed amine groups to conjugate to the surface carboxyl TG groups (Fig. S19). The resulting bilayers were highly deformable, as they could be strained to 1000% (Fig. 4b) and had an effective elastic modulus (E) that was almost 20-fold less than that of pure PEVM films, and only slightly larger than that of TG alone (Fig. 4c). These encapsulation materials had no detrimental impact on astrocyte viability (Fig. S17), and could be patterned with a CO_2 laser to create openings at the desired electrode sites without compromising the attachment process of the bilayer. The patterned encapsulation layers could also be stretched without tearing at the interface of the patterned portions (Fig. 4d).

Assembly of a fully viscoelastic device and *in vivo* validation

The process to fabricate a fully viscoelastic array is described in Fig. S20. The self-healing properties of PEVM enabled seamless integration of the two PEVM layers via hydrogen bonding. The completed device was viscoelastic and highly conformable (Fig. 5a). Further, the conductive tracks could be fabricated with stiffness and viscoelasticity that overlap with those of heart and brain tissue (Fig. 5b)[18,31–39]. This contrasts with previously described

electrical composites, which typically have much higher moduli and do not exhibit the viscoelasticity of tissues.

The electrical behaviour of devices was first characterized in phosphate buffer solution (PBS). The composition was cast in moulds with deeper electrode sites and a flexible comb-like connector was used to intimately contact each pad. The median impedance range at 1 kHz for 5 devices with 40 tracks was 167kΩ +/− 40kΩ, with an electrode surface area of 0.38 mm^2 (Fig. 5c). Intertrack resistance was 2–40MΩ in a hydrated environment, confirming no short-circuits between independent tracks (Fig. S21).

Impedance spectra at 1 kHz and intertrack resistance of four arrays was measured over time following submergence for 84 days at room temperature in PBS with 2 mM $CaCl_2$ (Fig. 5d). Three of the arrays had no significant change in impedance, and the intertrack resistance did not significantly change across any of the arrays. Further, all devices remained fully attached and with no changes in any dimensions. To mimic the effects of multiaxial mechanical cycling in a physiological system, a mouse was intubated and mechanically ventilated with the stroke volume set to correspond to 11% linear strain in each direction, similar to the physiological strain experienced by the mouse heart. An array was placed on the exposed muscle and cycled either 10,000 times or 100,000 times (Fig. 5e). All 24 electrodes cycled 10,000 times had less than a 2x increase in impedance. For the array cycled 100,000 times, only one electrode was visibly fractured. No array slipped, as the hydrogel encapsulation interfaced intimately with the hydrophilic tissue.

The viscoelastic array was fabricated to match the dimensions of a commercial array, and the conformability and functionality of the two were compared on a bovine heart (Fig. 5f). When both arrays were on a flat portion of the tissue, all 4 electrodes were in good contact and demonstrated a consistent impedance (105kW, 300W, viscoelastic and commercial electrodes, respectively). On the heart wall, where the arrays needed to bend more than 90°, no electrode of the commercial grid was in contact with the tissue. All 4 electrodes of the viscoelastic grid remained in contact and had no significant change in the impedance (Fig. S22). When bent >180° around the tissue, the viscoelastic array remained in contact, with no change in functionality (Fig. S23). The charge storage capacity (CSC) for the clinical-scale grids (electrode diameter=5 mm) was calculated over the voltage range that corresponded to the water window of each composition (Fig. 5g) and the carbon-based electrodes had more than 10x CSC than the platinum electrodes. This range was (−4V, 4V) for the nanomaterial electrodes, and (−1V, 1V) for the platinum electrodes, as the carbon tracks were highly resistive and thus required a larger applied voltage to reach water electrolysis at the electrode interface. As the relative ratios of GF and CNT were changed, the CSC was adjusted, which suggested that carbon additive composition can be tuned to achieve stimulation electrodes or recording electrodes (Fig. S24).

Arrays were placed on explanted tissues and conformed to the cortical surface of a rat brain, intimately covered a rat heart, and precisely wrapped around nerves in a bovine heart (Fig. 6a). There was no macroscopic damage caused to any of the structures, and no array components delaminated. To validate functionality *in vivo*, a mouse hindlimb was stimulated at various locations (Fig. 6b). The pulse parameters were kept constant, but the location

of the electrode or the electrode which applied stimulation were changed. This resulted in different responses, such as activation of the toes only, the ipsilateral foot only, the entire ipsilateral ankle, or both the ipsilateral and contralateral limbs (Supplemental Videos 1: toe activation, 2: foot activation).

Finally, we evaluated the recording capabilities of the viscoelastic array on the heart and brain in rodents. During acute *in vivo* surgeries, arrays were placed on the epicardial surface of the mouse heart, or on the epidural surface of the rat cortex. An 8-electrode array, as a 3×3 grid of electrodes with diameter of 700 μm and a spacing of 800 μm between adjacent electrodes and with the centre position left empty, was designed for these studies; larger arrays and more electrodes can be readily fabricated for studies with larger animals. The array stayed flat on the mouse heart and remained in place by surface tension and plastic deformation as the organ continued to beat (Fig. S25). We obtained electrocardiogram recordings (Fig. 6c), with a maximum signal-to-noise ratio (SNR) of 17.4. Next, the array was wrapped around the heart and recorded from the posterior side of the tissue, with the array bent more than 180° (Fig. 6d). The electrodes remained functional, with a SNR of 15.6. To confirm the signals recorded were specific to the heart, and not an artefact from the physical movement of the tissue, the grid was placed on the exposed liver, where no electrical signal was recorded (Fig. S26).

For neural recordings, the electrode array was placed on the dura of a Thy1 rat. This transgenic rat model was used as its neurons could be depolarized by directing a blue light laser beam at the cortex through the transparent portions of the viscoelastic grid (Fig. S27). First, the laser at 90 mW power was directed to the centre of the array, indicated in Fig. 6e, to induce electrical activity in the underlying cortex. All 8 electrode channels successfully recorded electrical activity (Fig. S28), and the traces over the recording session were averaged for each channel (n=63) and plotted (Fig. 6e). Signals with an amplitude of approximately 1 mV were recorded, and depolarization events which corresponded to the laser stimulation were reliably identified. Next, the laser position was moved to the left-lateral edge and the amplitude and waveform of the recorded activity were diminished. The neural activity recorded by the array was significantly reduced when the laser was directed to the lateral portion of the array, and the amplitude of the traces from both laser positions were reduced when the power was lowered to 45 mW. Finally, when the pulse duration of the laser increased from 5 to 10 ms, the time to electrical depolarization over the electrodes increased, and this trend was observed over three levels of laser power (Fig. S29). These experiments confirm the recorded activity was real signal based on the underlying neurons, as opposed to nonspecific tissue activity. Additionally, the amplitude of activity recorded is comparable to existing arrays with similar electrode diameters[6,13].

A 3-electrode viscoelastic array was also placed over the auditory cortex of a wild-type rat (Fig. 6f). This far lateral cortical target is surgically more difficult to access, and the device was bent more than 180°. The array remained functional, and all electrodes recorded auditory evoked potentials (AEP) in response to tone bursts from 1kHz to 10kHz frequency. The 3 electrodes displayed typical AEP at the onset and offset of the sound. Interestingly, the relative signal magnitude between the AEP amplitude at sound onset and offset differed amongst the three electrodes, which suggested that the electrodes were recording local

tonotopic information. Indeed, each electrode displayed a different frequency tuning profile with a maximum SNR of 18 for the recorded surface potentials.

Discussion

We report on the first fully viscoelastic electrode array, which exhibits a similar mechanical profile to soft biological tissues. The arrays are prepared from mostly hydrogels that have highly tuneable physical properties, and the viscoelasticity and stiffness can be independently varied. Additionally, these surface arrays featured novel electrical conductors made from low loading fractions of high aspect-ratio carbon nanomaterials, and thus retained an ultra-soft modulus and viscoelastic nature. Likely due to the matching of mechanical properties to neural tissue, neural cell responses to the soft viscoelastic array materials *in vitro* were favourable, with minimal astrocyte activation and enhanced neurite spreading. Further, high signal-to-noise ratio recordings of 18 were obtained *in vivo*, enabling the recording of low-amplitude local field potentials. Further, the electrode design and the array fabrication process are facile and fast (3 days from design to functional and fully assembled array) and do not require high temperatures, harsh chemical etchants, or thin-film photolithographic technologies. As the electrodes and tracks are made of the same composition, and due to the stability of the graphene and carbon nanotubes, there is no interface delamination or need for metallic films, thus presenting a class of arrays that would be compatible with a multitude of imaging techniques, such as MRI. Since different compositions of carbon additives demonstrated tunability of the charge storage capacity, a combination of different formulations can be used to fabricate one array that has some tracks more optimized for stimulation and others more optimized for recording.

This ultra-soft technology can likely be optimized in future bioelectronic interfaces, for both 2D and 3D microelectrode arrays, and become a useful tool to better understand how organs develop, function, and change throughout diseased states. A striking feature of the viscoelastic arrays is that they plastically deform upon implantation, enabling rapid ‘personalization’ to the local environment without the need for changing the electrode layout. The same initial 2D grid will quickly conform to the underlying tissue architecture without compromising the electrical and mechanical properties of the nanomaterial-based tracks. Implantation of the arrays in larger mammals, such as the porcine brain, would offer complex geometries (e.g, intrasulcular) for recordings, which are currently inaccessible without causing significant plastic damage to the tissue. As our arrays are currently limited by the track width of the electrodes due to the small anatomy of rodents, the technology would benefit from applications where the features could be scaled up. This could be done without increasing the overall thickness of the device nor compromising its viscoelastic nature.

MATERIALS AND METHODS

Animal tissue samples.

Sprague Dawley rats (female, 24 weeks of age, Charles River Lab) were euthanized in compliance with National Institutes of Health and institutional guidelines. Hearts were explanted immediately after euthanasia. Young lamb (6–8 weeks of age) whole brains

were obtained from the local butcher shop, within 2 hours of the animal being sacrificed. Samples were kept at room temperature and tested with a Discovery HR-2 rheometer (TA Instruments) within 12 hours of tissue acquisition.

Preparation of the alginate hydrogel substrates.

Sodium alginate with high molecular weight (Protanal LF 10/60, FMC Biopolymer) was used to prepare the ionically crosslinked alginate gels[40] and the tough interpenetrating networks[29], both as have been described previously. For certain studies, the polymer was irradiated by a 5 Mrad cobalt source to produce lower-molecular weight alginate, as previously described[40]. RGD-alginate was prepared by coupling the oligopeptide GGGRGDSP (Peptides International) to the sterile alginate using carbodiimide chemistry, as previously described[12]. To form substrates for cell experiments, alginate was weighed into sterile scintillation vials and media added so that the concentration of the alginate was 2.5% w/v. The vials were left overnight on a stir plate to allow the contents to dissolve completely. Sterilized calcium sulphate slurry was added to a sterile scintillation vial as well, and diluted 5x in the corresponding media. Crosslinked gels were fabricated, as previously described[12]. The Matrigel-alginate interpenetrating network gels were fabricated as previously described[7], using reduced growth-factor, phenol-free Matrigel (Corning, lot number 0083005).

Preparation of agarose brain samples.

MRI data from a healthy porcine brain (permission of NeuroScience Associates of Knoxville, Tennessee NSALabs.com, April 2018) was used to print a plastic version of the tissue (Formlabs Form 2 3D printer, Formlabs standard resin). Ecoflex 0030 (Smooth-On, Reynolds Advanced Materials) was moulded around the plastic and left overnight to fully crosslink. Agarose powder (≥99%, Sigma-Aldrich 9012-36-6) was mixed with water to make a 0.25% w/v solution, left at 4°C to allow the agarose to crosslink in the negative elastomeric mould. In certain studies, a drop of food colouring dye (McCormick, local grocery store) was added to the agarose solution before casting to provide contrast.

Assessing substrate colour conformability and movement.

Yellow agarose porcine brain models were prepared as described above. Alginate gels were prepared as per above, and dyed blue. Ecoflex 0030 films were spin coated (Laurell Technologies, Model WS-650-23) at 400 rpm (film thickness ~100 μm). Polyimide films of 25 μm were purchased (DuPont Kapton) cleaned with methanol (Sigma-Aldrich) and water, and dried. All substrate materials were laser cut to 10 mm × 20 mm rectangles. The Ecoflex and polyimide were coloured by painting blue hydrophobic silicone pigment (Smooth-On, Reynolds Advanced Materials) on the surface. All 3 substrate materials were implanted at two locations of the brain models: one at the anterior portion (low radius of curvature), and the second around the posterior portion (high radius of curvature). Every sample was placed medially-laterally (starting at the midline side, gently lowering towards the lateral brain). The alginate substrates were left in place for 90 seconds. The Ecoflex and polyimide samples were left for 5 minutes to allow ample time for dye transfer. The number of transferred blue pixels was quantified with ImageJ.

To explore long-term movement and conformability, substrates of alginate (300 μm) and Ecoflex 0030 (150 μm) were prepared, with the thicknesses chosen so the bending stiffness of each substrate, D,

$$D = \frac{E\,h^3}{12\left(1-\nu^2\right)}$$

was approximately the same. (SI Table 1).

Each substrate material was placed on a hemisphere of the brain models, at the posterior-most portion. A hydrophobic dye marked the original location of the substrate relative to the brain. All dishes were sealed with parafilm and placed on an orbital shaker (VWR Digital Shaker), at 37°C and 100 rpm to mimic the brain micromotion. After 14 days, the brain models were photographed before and after the substrates were removed. The substrates were also photographed upon removal to determine if they flowed over the two weeks to conform to where they were placed.

Cell culture studies.

Primary rat cortical astrocytes (Lonza, verified by the manufacturer to be negative for mycoplasma), were thawed and cultured in AGM (Astrocyte Growth Medium BulletKit, Lonza) following manufacturer's guidelines. Primary rat cortical neurons (Lonza, E18,19, verified by the manufacturer to be negative for mycoplasma) were thawed before use. NBM (Neurobasal Plus Medium with 2% B27, Lonza) was used to culture the cells, which were used directly after thawing.

Primary rat astrocytes (Lonza) in flasks were removed at P6, using 0.25% trypsin/EDTA (Sigma-Aldrich, washed once in AGM, resuspended in fresh AGM and seeded on top of the preformed gels a density of 40,000 cells/cm^2. The cells were left for 30 minutes in an incubator at 37°C to begin to attach to the gels, after which the remainder of AGM was added to each well, dropwise and to the outer portion of the well avoid disruption to the attached astrocytes. The cells were imaged every day, for 5 days, with an upright light microscope (EVOS).

Primary rat neurons (Gibco) were thawed directly before use, following manufacturer's guidelines, without centrifugation and by suspending the cells with gentle mixing by a P1000 pipette. Neurons were seeded on top of the preformed alginate-Matrigel IPN at a density of 62,500 cells/well (~90,000 cells/cm^2). The cells were left for 15 minutes in an incubator at 37°C to begin to attach to the gels, after which the remainder of NBM was gently added to each well, dropwise and to the corner of each well, so that the total volume of media was 400 μl. Five hours after seeding the neurons, half the NBM was carefully removed and fresh 200 μl was added. The neurons were imaged every day, for 8 days, with the EVOS.

For the coculture experiments, ~2 million primary rat astrocytes in flasks were removed at P7, and 1 million primary rat neurons were thawed. Both cell types were added to NBM and pipetted up and down to uniformly mix and added on top of the gels. After five hours of

seeding, half of the NBM was carefully removed and fresh 200 μl of media added. The cells were imaged every day, for 5 days, with the EVOS.

Immunostaining.

The astrocytes were incubated in 4% paraformaldehyde for 15 minutes at room temperature and washed several times using HBSS supplemented with 10 mM of $CaCl_2$. For antibody staining, the cells were permeabilized with 0.1% Triton X-100 in HBSS for 8 minutes, washed 6 times with HBSS with added calcium, and then incubated with blocking buffer (5% goat serum, 1% bovine serum albumin). Then, the cells and gels were incubated with an antibody against GFAP (Abcam, ab33922, concentration 1:300), MAP2 (Invitrogen, PA1-10005, concentration 1:5000), NeuN (Abcam, ab104224, concentration 1:1000), β3-tubulin (Abcam, ab18207, concentration 1:2000) overnight at 4°C. The next day, the samples were incubated with a fluorescently labelled secondary antibody (Alexa488, Abcam 1:500; goat anti-chicken Alexa 555 ab150170 1:500; goat anti-mouse Alexa 488 Invitrogen A-11029 1:500; goat anti-rabbit Alexa 555 ab150078 1:500) for 1 hour at room temperature. Staining for cell nuclei was performed with Hoechst 33342 (concentration 1:1000) for 10 minutes, at which point the samples were transferred to slides. Mounting media (Prolong Gold Glass Antifade, Invitrogen) was added, and a coverslip placed on top of the gels. Images were taken with a Leica SP5 X MP Inverted Confocal microscope at 4x, 10x, 20x, 40x oil, and 63x oil magnification. More than 10 random fields were taken per sample.

Fabrication of the viscoelastic insulation materials.

Physically entangled viscoelastic material (PEVM) was used to fabricate the insulation materials. In brief, amine-terminated polydimethylsiloxane (NH_2-PDMS-NH_2, aminopropyl-terminated polydimethysiloxane, 100–120 cSt, Gelest), methylenebis(phenyl isocyanate) (MPI, Sigma-Aldrich, 0.4 eq), and isophorone diisocyanate (IPDI, Sigma-Aldrich, 0.6 eq) were reacted as described previously to synthesize PDMS-MPU-IU, a robust self-healing material[30]. Then, PDMS-MPU-IU was dissolved in chloroform ($CHCl_3$, anhydrous, ≥,99%, Sigma-Aldrich) and placed on a shaker (ThermoFisher Scientific) overnight to create a uniform viscous solution, and NH_2-PDMS-NH_2 monomer was added to the dissolved PDMS-MPU-IU. The resulting solution was dispensed evenly onto the surface of a cleaned polyethylene terephthalate (PET, Sigma-Aldrich) film and left to crosslink for three hours at room temperature under ambient conditions. Then, the film was placed in an oven at 65°C to remove any traces of $CHCl_3$. The presence of exposed amine functional groups was confirmed using FTIR (Bruker Hyperion 3000 FTIR Microscope), for peaks around 3400 cm^{-1}.

Fabrication of the encapsulation materials.

To fabricate the encapsulation material, the tough gel and the PEVM film were covalently coupled using carbodiimide chemistry. EDC (N-(3-dimethylaminopropyl)-N'-ethylcarboiimide hydrochloride, Sigma-Aldrich) and sNHS (N-hydroscysulphosucinimide, ThermoFisher Scientific) were combined in a 1:1 ratio and a 0.1M MES (2-(N-morpholino)ethanesulfonic acid, Sigma-Aldrich) buffer adjusted to pH 6 was added, and the EDC and sNHS concentration was each 0.033 mg/μl. The resulting solution was dispensed

onto the surface of the tough gel, which was lowered onto the unmodified PEVM film and firmly pressed to remove any air bubbles and left overnight.

Fabrication of the conductive gels.

Both nanoporous and microporous conductive gels (nanoCG, microCG respectively) were fabricated with the same initial step of fabrication. Defects-free graphene flakes (GF, 1.39 mg/ml, Supplemental methods) and/or carbon nanotubes (CNT, NC3100 Nanocyl) were combined in 2% w/v alginate solution, the total contents briefly vortexed and then placed in a sonicator bath (Grainger Industrial Supplies). To form nanoCG, a dispensed amount of conductive gel solution was placed in a bath of 100 mM calcium chloride (calcium chloride dihydrate, Sigma-Aldrich) and rinsed with deionized water.

To fabricate the microCG, the well-mixed solution is dispensed onto a clean surface and rapidly moved to a freezer (−20°C, or −80°C). The frozen gels are moved to a lyophilizer (Freezone, Labconco) overnight. Once removed from the lyophilization tube, the dried gels are crosslinked with 100 mM calcium nitrate (Sigma-Aldrich) in ethanol and left for at least 30 minutes. The gels are then rinsed with 100% ethanol and dried again.

To characterize the electrical behaviour of the gels, 5 mm × 15 mm × 300 um conductive gels were cast in 3D printed moulds (Stratasys printer, Objet 30 pro). To fabricate electrical tracks that were integrated in a complete device, the gels were cast in 3D printed moulds that were 300 μm × 15 mm × 200 μm with a pad, 600 μm × 4 mm, and 700 μm diameter electrodes.

Patterning the encapsulation layer.

A Helix 75W laser (Epilog CO2 Laser Cutter), beam diameter 127 μm, was used to create openings of the encapsulation layer at the sites in which it was desired to have electrodes. The power was adjusted between 7–16% depending on the thickness of the layer, and the specific type of gel, with a speed at 30%, and a frequency of 420 Hz. All files were drawn in CoralDRAW (Graphic Design Software), and printed as hairline features.

Assembly of the complete device.

AutoCAD (Autodesk) software was used to design a positive mould of the electrical components (pads, tracks, and electrode sites) with the same dimensions as the final design. The electrode sites were extruded an additional 400 μm. Pieces were printed with a clear rigid photopolymer resin (PolyJet, Stratasys) using an Objet 30 pro 3D printer (Stratasys) and dried in an oven.

Ecoflex 0030 (Smooth-On) was mixed in a 1:1 ratio of A:B, and a small amount of blue hydrophobic dye (Smooth-On, Silicone Pigment) was added, cast over the positive moulds, and left at 65°C to crosslink for two hours to form a flexible negative mould of the design. Next, the entire length of the tracks was filled with a uniformly suspended conductive gel formulation and nanoCG or microCG were fabricated. The surface of the flexible mould was completely dried and then aligned with the PEVM-facing surface of the encapsulation and the crosslinked tracks were transfer printed onto the substrate. Finally, a connector with a 1

mm pitch (designed by Laboratory Soft Bioelectronics Interface, EPFL) to match the pitch of the pads was aligned with the pads, and the encapsulation housing piece was aligned from the electrode sites, to the connector. The encapsulation layer covered the connector, and the assembled device was left for 24–48 hours to allow the PEVM layers to self-heal together. A large 2 mm × 3 mm glass slide was left over the encapsulation piece to accelerate the self-healing process.

Mechanical testing.

All tests were performed in ambient conditions. To measure the rheological properties of the tissue (lamb cortex, rat heart), and all synthetic materials (ionically crosslinked alginate, tough gel, agarose gels, conductive gel formulations), a Discovery HR-2 rheometer (TA Instruments) with a 20 mm flat plate geometry was used to test all samples with the same procedure file. The gap of the two plates was always greater than 2 mm (2430 μm on average), and all samples tested were trimmed as needed so that they did not spill over when compressed. The synthetic gels were cast in a 12 well non-tissue culture plate, well diameter 20 mm. The rheometer stage was 37°C and a strain sweep test (at 1 Hz) was test on each sample was followed by a frequency sweep test (at 0.5% strain). No prestress was applied to any sample for any measurement If a sample failed to completely fill the gap spacing, it was discarded.

To evaluate the surface properties of the tissues and the hydrogels, a nanoindentator G200 (Keysight Technologies) with a flat punch (98 μm) tip was used. At least 5 measurements per sample were taken, and no more than 10 measurements, to minimize potential effects of the sample drying. After every 5 samples were tested, the tip was cleaned to remove any residues or aggregates from the previous samples.

Evaluation of the PEVM, Ecoflex, PEVM/TG composite, and tough gel films was also done with a tensile machine (Instron model 3342) with a 50N load cell. All samples were laser cut to the same gauge length of 5 mm. Thin (25 μm) films of polyacrylic were placed on either side and at both ends of the rectangular samples to prevent slippage. After the films were secured, the load cell moved upwards at a rate of (1 mm/s) until the film fractured. The elongation (mm) and stress (MPa) were recorded. Using the initial linear region of the resulting stress-strain graph, the elastic modulus of each material was extracted.

Structural characterization.

SEM of the samples was done using a Hitachi SU8230 Field Emission scanning electron microscope. The samples were completely dried, mounted on small SEM stubs (Ted Pella) with carbon tape (Ted Pella), and then 5 nm of Pt/Pd 80/20 (EMS 300T D Dual Head Sputter Coater, Quarum/EMS) was deposited on the surfaces at a current of 40 mA.

Porosity characterization.

Conductive gels of various compositions were cast and crosslinked, predominately with the microCG method. The gels were placed in DI water, and then onto a dry plastic dish to remove any excess water. The mass of the gels was calculated, in the hydrated state. Next, the water was wicked away with a Kimwipe so that the water in the pores was removed. The

gels were weighed again, and the difference in mass divided by the final mass was the % porosity of the samples.

Resistance and conductivity characterization.

The resistance of freestanding tracks with varying amounts of GF and/or CNT with dimensions of 400 μm × 15 mm and a thickness of 200 μm was measured using a four-point probe method with a Hioki RM3544 Resistance Meter under ambient conditions. The conductivity was calculated using the following formula[41]:

$$\sigma = \frac{S}{twR}$$

where σ is the calculated conductivity (S/m), s is the spacing of the pins of the 4-point probe (2.54 mm), t is the thickness of the gel measured (250 μm), and w is the width of the gel (400 μm). To confirm the calculated σ values, the resistance of a subset of larger samples (5 mm × 15 mm × 200 μm) was measured and the conductivity compared. A multimeter (Digilent Inc, Digikey) was used to measure the intertrack resistance using DC current.

Impedance characterization and cyclic voltammetry.

A ZIF connector (designed by LSBI to match the corresponding ribbon cable connector) was connected to the free-end of the connector. The PalmSens4 (PalmSens, Netherlands) potentiostat was used to record the impedance of exposed electrode through the entire length of the electrical track (15–20 mm). The working electrode of the PalmSens was connected to a jumper cable that was able to clip to each respective pin of the ZIF. A platinum counter electrode (BioLogic) with a surface area of 0.7 cm^2 was used, and a silver/silver chloride reference electrode (Ag/AgCl) (Ohaus 30059253). The impedance behaviour was characterized over a frequency sweep from 1 MHz to 1 Hz, with 10 points per decade. The PalmSens4 was also used to assess the electrode stability with cyclic voltammetry. 3 scans were performed at a rate of 0.1 V/s, typically with a range from −1V to 1V. This voltage range was increased to −4V to 4V when trying to find the water window of some of the carbon-based conductive gel formulations.

Ageing of the arrays.

Fully assembled arrays were placed in a petri dish that contained PBS with 2 mM $CaCl_2$, with the $Ca2^+$ added to prevent the alginate gels from dissociation, and then sealed with parafilm to prevent the solution from drying out. After 84 days, the devices were removed and the impedance spectra and intertrack resistance measured. The device was placed such that the connector end, which plugs into the ZIF board was not in contact with the saline solution, as it would have affected the functionality of the pins.

All animal procedures were done in compliance with National Institute of Health and Institutional guidelines with approval by Harvard University Institutional Animal Care and Use Committee. A mouse was terminally anesthetized and then intubated with a MiniVent ventilator for mice (Model 845). The fur was removed, and blunt dissection used to expose the muscle underneath. Each array was placed directly on top of the rib cage, and PBS added

to keep the array hydrated. The stroke volume was set to 250 μl and to 150–200 strokes/min, and left for 90 minutes (~10,000 cycles) or 6 hours (~100,000 cycles). The impedance spectra were measured after the cycling, and the impedance at 1 kHz was normalized to the impedance spectra at 1 kHz before the cycling (Day 84/Day 0).

In vivo validation.

All animal procedures were done in compliance with National Institute of Health and Institutional guidelines with approval by Harvard University Institutional Animal Care and Use Committee, or the Veterinary Office of the canton of Geneva in Switzerland. For the cardiac studies, two C57BL/6J (Jackson Laboratory) 18 week old male mice were euthanized with $C0_2$ and then immediately placed on a warm pad with sterile gauze. A clean device was placed on the surface of the heart and connected to a compatible custom-made PCB with 32 pins. Clips were connected to the pins, and to the cut ends of a sensor cable electrode pad (CAB-12970 ROHS, SparkFun). The electrode cable connected to a soldered AD8232 Heart Rate Monitor board (SparkFun). The AD8232 Heart Monitor connected to a computer via USB connection, and a custom Matlab code was used to visualize and save each recording session. After the recordings, the files were processed using a custom Matlab code, with a Savitzky-Golay filter. The raw and filtered files were saved, and each EKG was superimposed, averaged, and saved. A control experiment was done recording from the device in air, and in contact with the exposed liver of the mouse.

The neural recordings were done in Geneva, Switzerland under the compliance with all relevant regulations, under the license GE 174_17. A W-Tg (Thy1-COP4/YFP) (NBRP 0685, Kyoto, Japan) transgenic female adult rat (~300 g body weight) was anesthetized with a mix of Ketamine (50–90 mg/kg) and Xylazine (5–10 mg/kg) diluted in NaCl before being head-fixed into a stereotaxic frame (David Kopf Instruments). A small craniotomy was performed, and the ECoG array was placed epidurally onto the cortical surface, such that the 8 electrodes were in intimate contact with the exposed tissue. The array had the same connector-PCB set-up described above, and the PCB was then connected to a pre-amplifier (MCS Wireless HS-32). A diode-pumped solid-state blue laser (473 nm, Laserglow Technologies) was coupled with a FC/PC terminal, connected to a 200 μm core optical fiber (ThorLabs), to deliver optical stimulation. The fibre was placed at the centre of the electrode grid and positioned using a micromanipulator. A silver ground wire was fixed to the skull using a metallic screw. Optical stimulation was delivered through the transparent viscoelastic device, in order to stimulate the cortical surface. The laser frequency was 2 Hz, with a 5 or 10 ms duration, and the intensity varied from 35 to 90 mW. The differential recordings triggered by the laser stimulation were performed with a custom code, implemented with a wireless amplifier system (Multichannel Systems Wireless W2100), at a sampling rate of 2 kHz, and a digital butterworth bandpass filter of 1–200 Hz. The recorded signals were averaged over each individual optical pulse, across 13 recording sessions which were each ~2 minutes. The procedure was repeated for 2 viscoelastic arrays, changing the orientation of the device on the cortex as well as the location of the laser stimulation. A control experiment with an agarose brain, and the same set-up described above, to exclude any signal generation due to a photoelectric effect.

For the auditory evoked potentials measurements, a wild-type female adult rat (200 g body weight) was anesthetized with a mix of ketamine (100 mg kg-1 body weight) and xylazine (10 mg kg-1 body weight, dilution with saline) before being head-fixed into a stereotaxic frame (David Kopf Instruments). After removing the temporal muscle, a small craniotomy was performed on the temporal lobe over the auditory cortex (A/P = −2.7 mm to −5.8 mm, M/L = +/− 6.4 mm to +/− 8.67 mm from bregma), the dura mater was removed and a smaller (3 electrode) viscoelastic ECoG device was placed subdurally onto the cortical surface, such that electrodes were in intimate contact with the exposed tissue. The ground was a metallic screw inserted over the frontal part of the brain through the skull. The differential recordings were performed with a wireless amplifier system (Multichannel Systems Wireless W2100), at a sampling rate of 2 kHz over a frequency range of 1–90 Hz. The auditory stimulation was performed using a free-field speaker playing ~120 tone bursts repeat at a frequency of 1 Hz (500ms on, 500ms off) over multiple sessions varying the sound frequency (baseline, 1, 2, 5 and 10kHz). The auditory evoked potentials were averaged over all epochs per frequency to display the average and standard deviation for each experimental set. Three different sets of devices were tested sequentially.

For the muscular stimulation, C57BL/6J (Jackson Laboratory) 20 week-old female mice were anesthetized with isoflurane, and then cervically dislocated. The skin over the hindlimb was removed, and the gastrocnemius exposed. An array was placed over the muscle, and connected to a function generator (33210A, Keysight). A needle was inserted under the skin of the mouse. Pulses of 300 μs width, and voltage intensity from 0 to 3 V, were applied every 1, 2, or 5 seconds. The electrode which applied the stimulation was changed, and/or the device was repositioned, to stimulate either a single digit, the foot only, the ankle only, the entire limb (ipsilateral) only, or both the ipsilateral and contralateral limbs. The stimulation was confirmed with at least 3 electrodes from 3 devices.

Statistical analysis.

Statistical analysis was done with GraphPad Prism9 software. One-way ANOVA and Tukey HST post hoc tests were done to compare different conditions. 5–15 random fields of view, at least, for image comparisons were taken and quantified.

Data availability:

The data sets generated during and/or analysed during the current study are available from the corresponding author upon reasonable request. Figure 6 has associated raw data (the electrocorticography recordings), as shown in the supplemental information Fig S28, and the raw files are available upon request.

Code availability:

There is no custom code deemed central to the conclusions. Questions about the code used to process the data can be directed to the authors and made available upon reasonable request.

Supplementary Material

Refer to Web version on PubMed Central for supplementary material.

Acknowledgements:

The authors thank Ted Sirota and Paul Machado, both at the Wyss Institute, Boston Massachusetts, for their help with 3D printing and machining of moulds, respectively. This work was supported in part by the Center for Nanoscale Systems at Harvard University, which is a member of the National Nanotechnology Infrastructure Network, which is supported by the National Science Foundation under award no. 1541959. We thank the Weitz lab for the use of their rheometer, which is funded by Materials Research Science and Engineering Center of Harvard University under National Science Foundation award no. DMR-1420570. This work was supported by an NSF GRFP to CMT, as well as funding for CMT by NIH grant awarded to DJM (RO1DE013033), NSF MRSEC award DMR 14-20570, and funding by the Wyss Institute for Biologically Inspired Engineering at Harvard University. Support for IdL was provided by the National Cancer Institute of the National Institutes of Health under Award Number U01CA214369. The content is solely the responsibility of the authors and does not necessarily represent the official views of the National Institutes of Health. HW gratefully acknowledges funding support from the Wyss Technology Development Fellowship. BRS is supported by National Institute of Dental & Craniofacial Research (R01DE013349) and the Eunice Kennedy Shriver National Institute of Child Health & Human Development (P2CHD086843). This work has received funding for AEA from the European Union's Horizon 2020 research and innovation programme under the Marie Sklodowska-Curie grant agreement No. 798504 (MECHANOSITY). KK, CC and YY mainly funded this work by the EPSRC Programme Grant 2D-Health (EP/P00119X/1). CC acknowledges support by the EPSRC (EP/N010345/1). NV, AT, FF and SPL were funded by the Bertarelli Foundation, the Wyss Center Geneva, and the SNSF Sinergia grant no. CRSII5_183519.

References

1. Tolstosheeva E et al. A multi-channel, flex-rigid ECoG microelectrode array for visual cortical interfacing. Sensors (Switzerland) 15, 832–854 (2015).
2. Luan L et al. Ultraflexible nanoelectronic probes form reliable, glial scar–free neural integration. Sci. Adv. 3, (2017).
3. Tybrandt K et al. High-Density Stretchable Electrode Grids for Chronic Neural Recording. Adv. Mater. 30, (2018).
4. Konerding WS, Froriep UP, Kral A & Baumhoff P New thin-film surface electrode array enables brain mapping with high spatial acuity in rodents. Sci. Rep. 8, 1–14 (2018). [PubMed: 29311619]
5. Lacour SP, Courtine G & Guck J Materials and technologies for soft implantable neuroprostheses. Nat. Rev. Mater 1, (2016).
6. Minev IR et al. Electronic dura mater for long-term multimodal neural interfaces. Science (80-.). 347, 159–163 (2015).
7. Chaudhuri O et al. Extracellular matrix stiffness and composition jointly regulate the induction of malignant phenotypes in mammary epithelium. Nat. Mater. 13, 970–978 (2014). [PubMed: 24930031]
8. Budday S et al. Region- and loading-specific finite viscoelasticity of human brain tissue. Pamm 18, 3–4 (2018).
9. Wang Z, Golob MJ & Chesler NC Viscoelastic Properties of Cardiovascular Tissues. in Viscoelastic and Viscoplastic Materials (InTech, 2016). doi:10.5772/64169.
10. Boyle NG & Shivkumar K Epicardial interventions in electrophysiology. Circulation 126, 1752–1769 (2012). [PubMed: 23027811]
11. Chaudhuri O et al. Substrate stress relaxation regulates cell spreading. Nat. Commun. 6, 1–7 (2015).
12. Chaudhuri O et al. Hydrogels with tunable stress relaxation regulate stem cell fate and activity. 15, 326–334 (2016).
13. Rubehn B, Bosman C, Oostenveld R, Fries P & Stieglitz T A MEMS-based flexible multichannel ECoG-electrode array. J. Neural Eng. 6, 036003 (2009). [PubMed: 19436080]
14. Bramini M et al. Interfacing Graphene-Based Materials With Neural Cells. Front. Syst. Neurosci 12, (2018).

15. Kostarelos K & Novoselov KS Graphene devices for life. Nat. Nanotechnol. 9, 744–745 (2014). [PubMed: 25286265]
16. Martín C, Kostarelos K, Prato M & Bianco A Biocompatibility and biodegradability of 2D materials: graphene and beyond. Chem. Commun. 55, 5540–5546 (2019).
17. Pampaloni NP, Giugliano M, Scaini D, Ballerini L & Rauti R Advances in Nano Neuroscience: From Nanomaterials to Nanotools. Front. Neurosci. 12, (2019).
18. Lu B et al. Pure PEDOT:PSS hydrogels. Nat. Commun. 10, 1043 (2019). [PubMed: 30837483]
19. Liu Y et al. Morphing electronics enable neuromodulation in growing tissue. Nat. Biotechnol. 38, 1031–1036 (2020). [PubMed: 32313193]
20. Yuan X, Wei Y, Chen S, Wang P & Liu L Bio-based graphene/sodium alginate aerogels for strain sensors. RSC Adv. 6, 64056–64064 (2016).
21. Golafshan N, Kharaziha M & Fathi M Tough and conductive hybrid graphene-PVA: Alginate fibrous scaffolds for engineering neural construct. Carbon N. Y. 111, 752–763 (2017).
22. Lin X et al. A viscoelastic adhesive epicardial patch for treating myocardial infarction. Nat. Biomed. Eng. 3, 632–643 (2019). [PubMed: 30988471]
23. Son D et al. An integrated self-healable electronic skin system fabricated via dynamic reconstruction of a nanostructured conducting network. Nat. Nanotechnol. 13, 1057–1065 (2018). [PubMed: 30127474]
24. Masvidal-Codina E et al. High-resolution mapping of infraslow cortical brain activity enabled by graphene microtransistors. Nat. Mater. 18, 280–288 (2019). [PubMed: 30598536]
25. Green R Elastic and conductive hydrogel electrodes. Nat. Biomed. Eng. 3, 9–10 (2019). [PubMed: 30932070]
26. Choi S et al. Highly conductive, stretchable and biocompatible Ag–Au core–sheath nanowire composite for wearable and implantable bioelectronics. Nat. Nanotechnol. 13, 1048–1056 (2018). [PubMed: 30104619]
27. Lee S et al. Ultrasoft electronics to monitor dynamically pulsing cardiomyocytes. Nat. Nanotechnol. 14, 156–160 (2019). [PubMed: 30598525]
28. Lee KY & Mooney DJ Alginate: Properties and biomedical applications. Prog. Polym. Sci. 37, 106–126 (2012). [PubMed: 22125349]
29. Sun JY et al. Highly stretchable and tough hydrogels. Nature 489, 133–136 (2012). [PubMed: 22955625]
30. Kang J et al. Tough and Water-Insensitive Self-Healing Elastomer for Robust Electronic Skin. Adv. Mater. 30, (2018).
31. Tondera C et al. Highly Conductive, Stretchable, and Cell-Adhesive Hydrogel by Nanoclay Doping. Small 15, 1901406 (2019).
32. Kim N et al. Elastic conducting polymer composites in thermoelectric modules. Nat. Commun. 11, 1424 (2020). [PubMed: 32188853]
33. Wang Y et al. A highly stretchable, transparent, and conductive polymer. Sci. Adv. 3, e1602076 (2017). [PubMed: 28345040]
34. Feig VR, Tran H, Lee M & Bao Z Mechanically tunable conductive interpenetrating network hydrogels that mimic the elastic moduli of biological tissue. Nat. Commun. 9, 2740 (2018). [PubMed: 30013027]
35. Vicente J, Costa P, Lanceros-Mendez S, Abete JM & Iturrospe A Electromechanical properties of PVDF-based polymers reinforced with nanocarbonaceous fillers for pressure sensing applications. Materials (Basel). 12, (2019).
36. Chen Z et al. Three-dimensional flexible and conductive interconnected graphene networks grown by chemical vapour deposition. Nat. Mater. 10, 424–428 (2011). [PubMed: 21478883]
37. Bhagavatheswaran ES et al. Construction of an Interconnected Nanostructured Carbon Black Network: Development of Highly Stretchable and Robust Elastomeric Conductors. J. Phys. Chem. C 119, 21723–21731 (2015).
38. Haggenmueller R, Gommans HH, Rinzler AG, Fischer JE & Winey KI Aligned single-wall carbon nanotubes in composites by melt processing methods. Chem. Phys. Lett. 330, 219–225 (2000).

39. Chen Y et al. A Skin-Inspired Stretchable, Self-Healing and Electro-Conductive Hydrogel with a Synergistic Triple Network for Wearable Strain Sensors Applied in Human-Motion Detection. Nanomaterials 9, 1737 (2019).

40. Rowley JA, Madlambayan G & Mooney DJ Alginate hydrogels as synthetic extracellular matrix materials. Biomaterials 20, 45–53 (1999). [PubMed: 9916770]

41. Topsoe H Geometric factors in four point resistivity measurement. Bulletin No. 472–13. (1966).

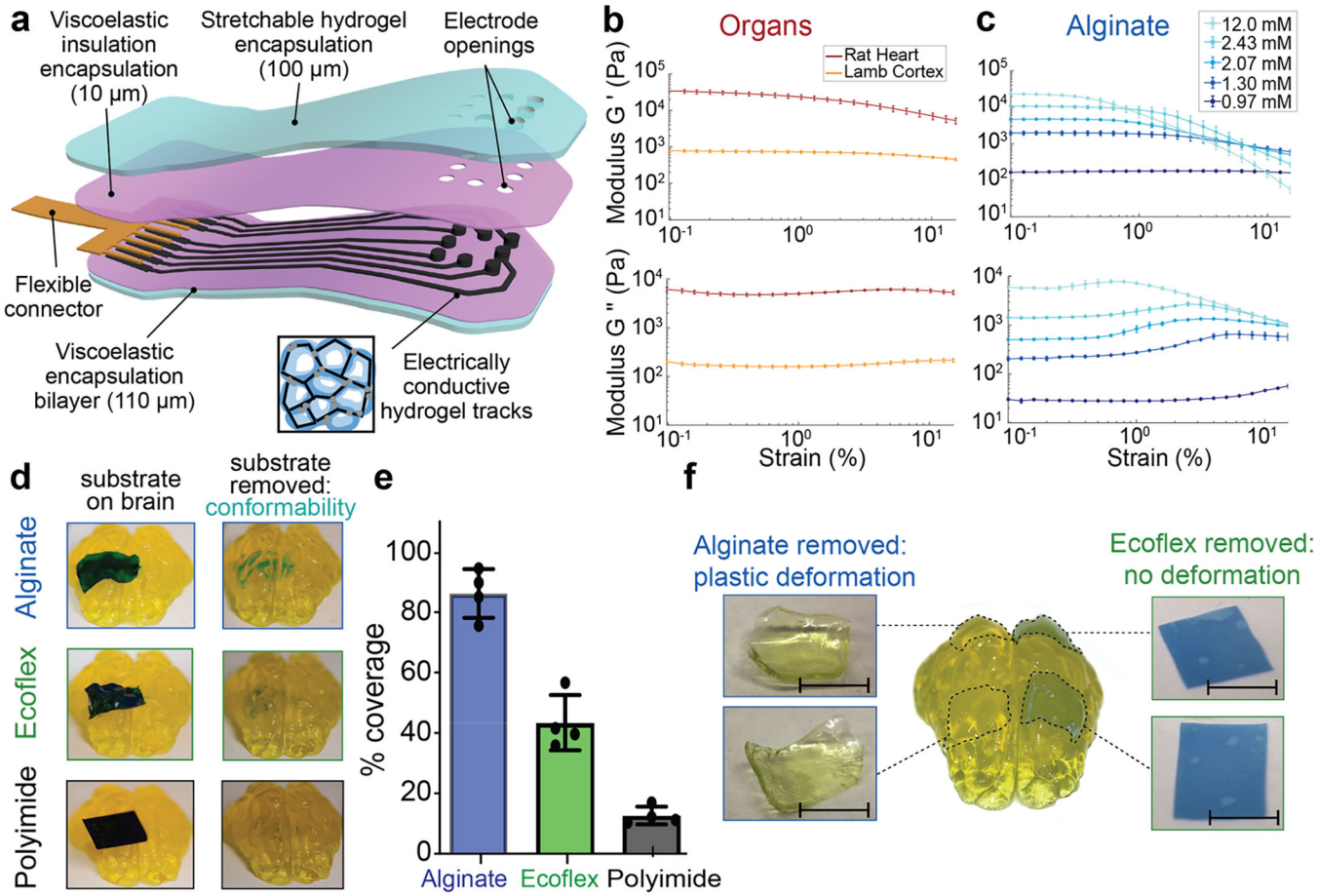

Figure 1: Alginate hydrogels match the viscoelastic properties of mammalian tissues and conform to complex substrates.

(a) Schematic of the proposed device and its various components. The encapsulation layer is made from a stretchable hydrogel (blue) to which a viscoelastic electrically insulating polymer (pink) is covalently coupled. The conductive tracks (black) are fabricated from a macroporous hydrogel with carbon additives (inset), and interface with a flexible connector (gold). As all the components of the device are viscoelastic, the assembled array can be designed to match the modulus, and flow to conform to follow the tissue on which it is implanted.

(b) Rheological properties of fresh lamb cortical tissue and fresh rat cardiac tissue. Storage moduli (G') (top), and loss moduli (G") (bottom) shown as a function of strain (ε), at a frequency of 1 Hz, n=10 independent tissue sample sections. Mean and s.d. are plotted.

(c) Rheological properties of alginate hydrogels with varying levels of crosslinking agent indicated in the legend. Storage moduli (G') (top), and loss moduli (G") (bottom) shown as a function of strain (ε), at a frequency of 1 Hz, n=8 independent gels of each formulation. Mean and s.d. are plotted.

(d) Photographs of plastic (5 mm × 15 mm × 25 μm sheet of polyimide, bottom), elastomer (5 mm × 15 mm × 100 μm sheet of Ecoflex, centre), and viscoelastic (5 mm × 15 mm × 250 μm sheet of alginate, top) substrates, with the thickness adjusted so that the bending stiffnesses were comparable. Substrates were coated with blue dye prior to application,

and images (left) demonstrate the shapes taken by each material immediately following placement onto the agarose brain model and images (right) after removal of the substrates, and the dye transferred from each substrate to the tissue demonstrated regions of close contact.

(e) Quantification of the area on model brains to which dye was transferred for each material (plastic, elastic, viscoelastic), as a metric of direct contact between the substrates and the porcine brain model. Values are normalized to that of the viscoelastic alginate substrate (n=3 substrates of each material).

(f) Photographs of viscoelastic (alginate sheets, 5 mm × 5 mm × 200 μm) and elastic (Ecoflex sheets, right: 5 mm × 5 mm × 100 μm) substrates, both when present on the porcine brain model and immediately after removal. The two substrates had matched bending stiffness and were placed on the brain models for two weeks prior to removal and immediate imaging. Scale bar represents 5 mm.

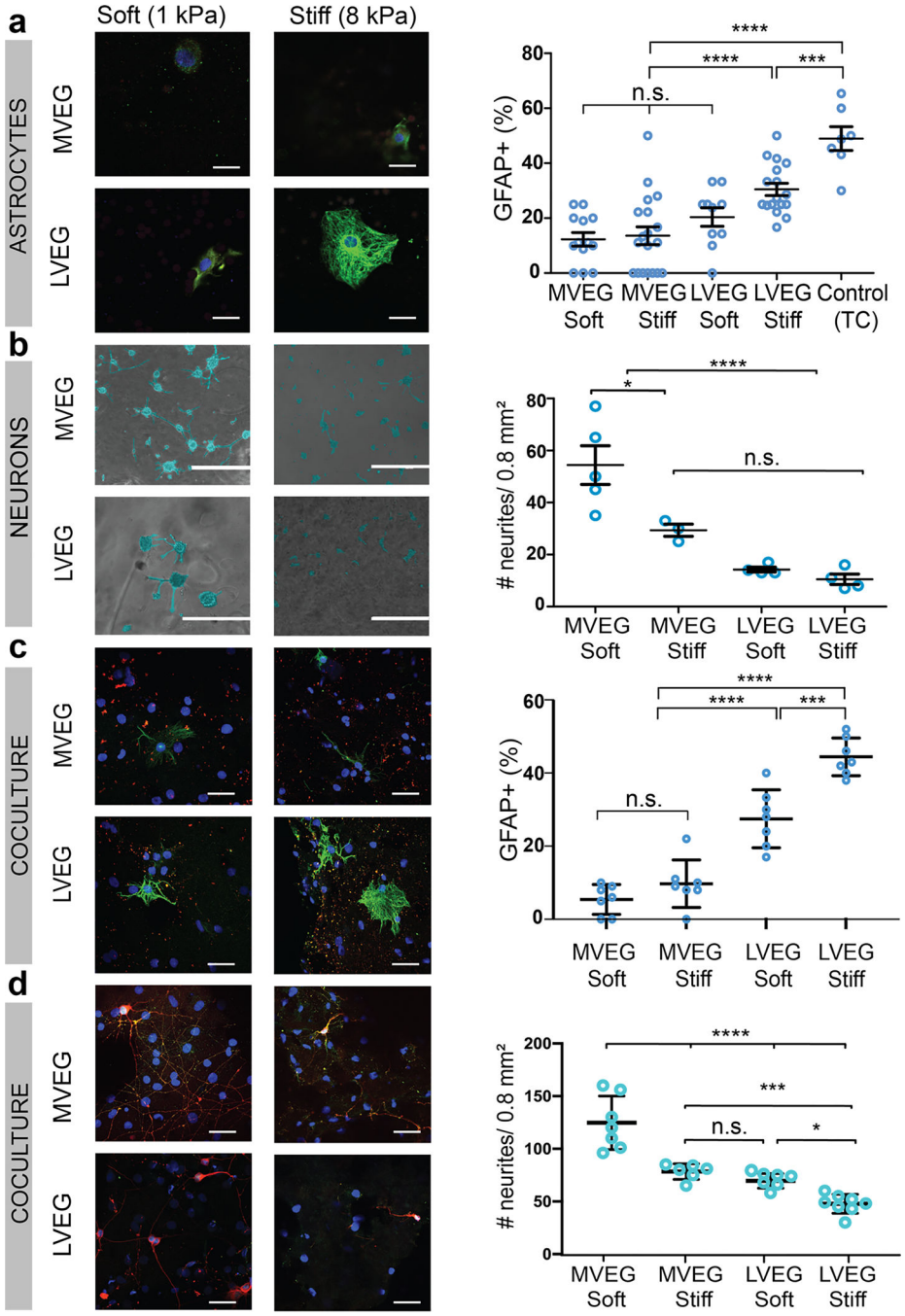

Figure 2: Alginate hydrogels can be tuned to optimize compatibility with both astrocytes, neurons, and a coculture.

(a) Photomicrographs of primary cortical astrocytes seeded on gels of different viscoelasticity (more viscoelastic gels, MVEG; less viscoelastic gels, LVEG) and stiffness (soft, 1 kPa, and stiff, 8 kPa), after 120 hours. Cells stained for GFAP (green)/nuclei (blue), scale bar represents 10 μm (left). Quantification of % cells positive for GFAP on each substrate (right) (n=4/sample, 14 random fields/sample) (p(***)=0.0021).

(b) Photomicrographs of primary cortical neurons seeded on alginate-Matrigel interpenetrating networks (IPNs) of different viscoelasticity (MVEG, LVEG) and stiffness

(soft, 1 kPa, and stiff, 8 kPa), after 72 hours. Cell bodies and neurites are falsely coloured blue to provide better contrast from the underlying gel. Scale bar represents 400 μm (left). Quantification of the number of neurites in a 0.8 mm^2 area (right) (n=4/sample, 5 random fields/sample) (p(*)=0.0194).

(c) Photomicrographs of a coculture of primary cortical astrocytes and primary cortical neurons, seeded on alginate-Matrigel IPNs of different viscoelasticity (MVEG, LVEG) and stiffness (soft, 1 kPa, and stiff, 8 kPa), after 120 hours. Cells stained for GFAP (green)/MAP2 (red)/nuclei (blue), scale bar represents 40 μm (left). Quantification of % cells positive for GFAP on each substrate (right) (n=4/sample, 8 random fields/sample) (p(***)=0.0018).

(d) Photomicrographs of a coculture of primary cortical astrocytes and primary cortical neurons, seeded on alginate-Matrigel IPNs of different viscoelasticity (MVEG, LVEG) and stiffness (soft, 1 kPa, and stiff, 8 kPa), after 120 hours. Cells stained for NeuN (green)/β3-tubulin (red)/nuclei (blue), scale bar represents 40 μm (left). Quantification of the number of neurites in a 0.8 mm^2 area (right) (n=4/sample, 7 random fields/sample) (p(*)=0.0238, p(***)=0.0035).

All numerical data are presented as mean ± s.d. (one-way ANOVA and Tukey's HSD post hoc test, ****p<0.0001, 0.0001<***p<0.001, 0.001<**p<0.01, 0.01<*p<0.05, and non-significant, n.s., p>0.05).

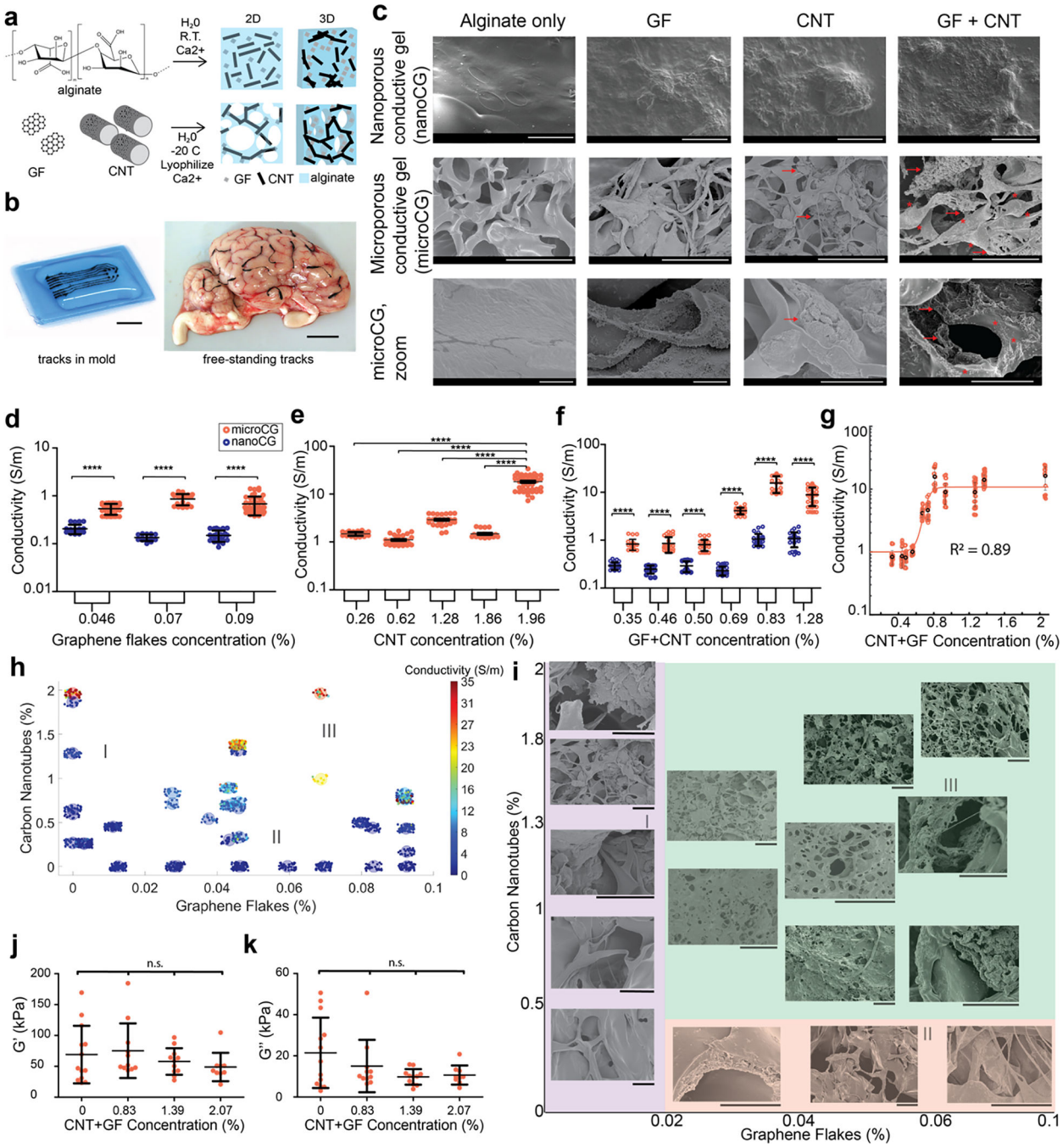

Figure 3: Viscoelastic electronics formed from an alginate matrix with electrically active carbon-based fillers.

(a) Schematic showing the fabrication of nanoporous conductive gels (nanoCG) and microporous conductive gels (microCG). An alginate solution, graphene flakes (GF), and/or carbon nanotubes (CNT) were mixed, and immediately crosslinked to create nanoCG (top) (pore diameter ~ 10s nm. When the mixed solution was frozen and lyophilized, a microCG (bottom) (pore diameter ~ 100s μm) was formed, with a higher density of carbon additives in the gel walls.

(b) Photograph demonstrating casting of the tracks in a flexible mold (left), and their ability to follow the vasculature of a fresh lamb brain. Scale bars represent 10 mm.
(c) Scanning electron microscope (SEM) photomicrographs comparing nanoCG (top row, scale bar: 100 μm), and microCG (middle row, scale bar: 50 μm), with no additives, GF-only, CNT-only, and GF+CNT. Higher magnification of microCG (bottom row, scale bar: 5 μm). Red arrows point to CNT, and * regions indicate regions containing GF.
(d-f) Quantification of the conductivity (S/m) of nanoCG (blue) and microCG (red), comparing the behaviour of GF-only (d), CNT-only (e), and GF+CNT (f) compositions at increasing concentrations of carbon (n=38 independent gels) and s.d (error bars) shown in black, with all p(****)<0.0001.
(g) Quantification of conductivity of microCG as a function of total carbon (GF+CNT) compositions, fit with a sigmoidal curve (R^2=0.89).
(h) Graphical evaluation of the relative contribution of GF (x-axis) and CNT (y-axis) on the conductivity of microCG. Resulting gel conductivity shown by color, ranging from low (blue) to high (red), as indicated in legend. (I), (II), and (III) marks regions of mostly CNT, mostly GF, and a mix of GF+CNT, respectively. Each small solid circle represents an independent gel measurement, and the coloration of the groupings of solid circles represents mean conductivity (n=20–30/composition).
(i) SEM photomicrographs comparing the structure of microCG at varying concentrations of only CNT, only GF, and a mix of GF+CNT. (I, purple), (II, red), and (III, green) marks regions of mostly CNT, mostly GF, and a mix of GF+CNT, respectively. Scale bar represents 20 μm in all images.
(j-k) Quantification of the storage modulus (G') (i) and loss modulus (G") (j) of GF+CNT microCG using nanoindentation (n=10 independent gels). All conditions were n.s.
All numerical data are presented as mean ± s.d. (one-way ANOVA and Tukey's HSD post hoc test, ****p<0.0001 and non-significant, n.s., p>0.05). Micrographs were repeated with at least 3 independent gels.

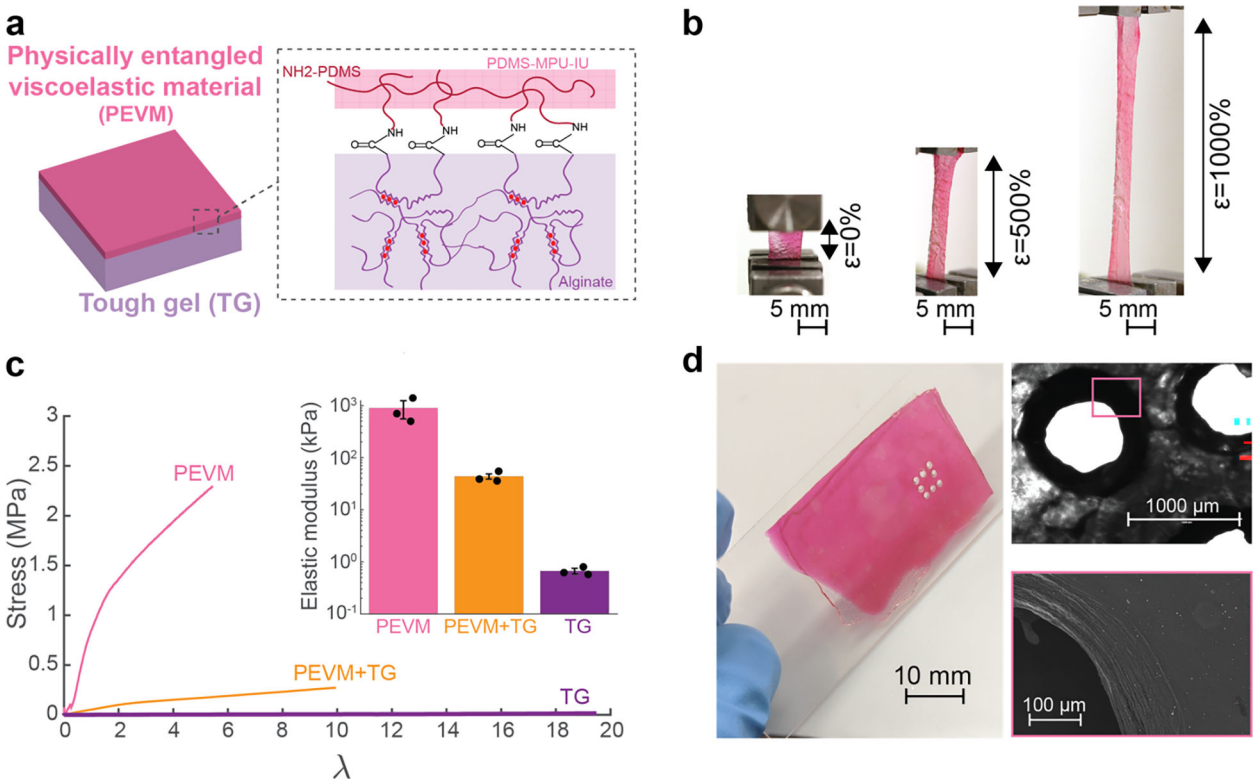

Figure 4: Fabrication of highly flexible and stretchable viscoelastic encapsulation layers.

(a) Schematic of the two individual components that comprise the encapsulation layers of the device. A stretchable alginate tough gel, TG (purple), was covalently coupled to a self-healing, PDMS-based, physically entangled viscoelastic material, PEVM (pink), via carboxyl-amine chemistry.

(b) Photographs of the composite encapsulation layer stretched under tension to 0, 500 and 1000% of the original length. The PEVM (pink) can be observed to begin to fracture at the greatest strain, while the TG (clear) remained intact. Scale bar represents 5 mm.

(c) Quantification of the stress (σ) vs elongation (λ) behaviour until the first point of film fracture. Representative curve shown for each encapsulation layer tested: PEVM-only, TG-only, and PEVM-TG (left). The elastic modulus for each material was extracted from the linear regime. Values represent mean (n=3 independent materials of each condition) and s.d. (right, inset).

(d) Photographs of the encapsulation layer following cutting with a CO_2 laser (left), bright field microphotograph (right, top) and scanning electron microscopy (SEM) view (right, bottom) of the cut after exposure to the laser. Scale bar represents 10 mm (left), 1 mm (right, top) and 100 μm (right, bottom).

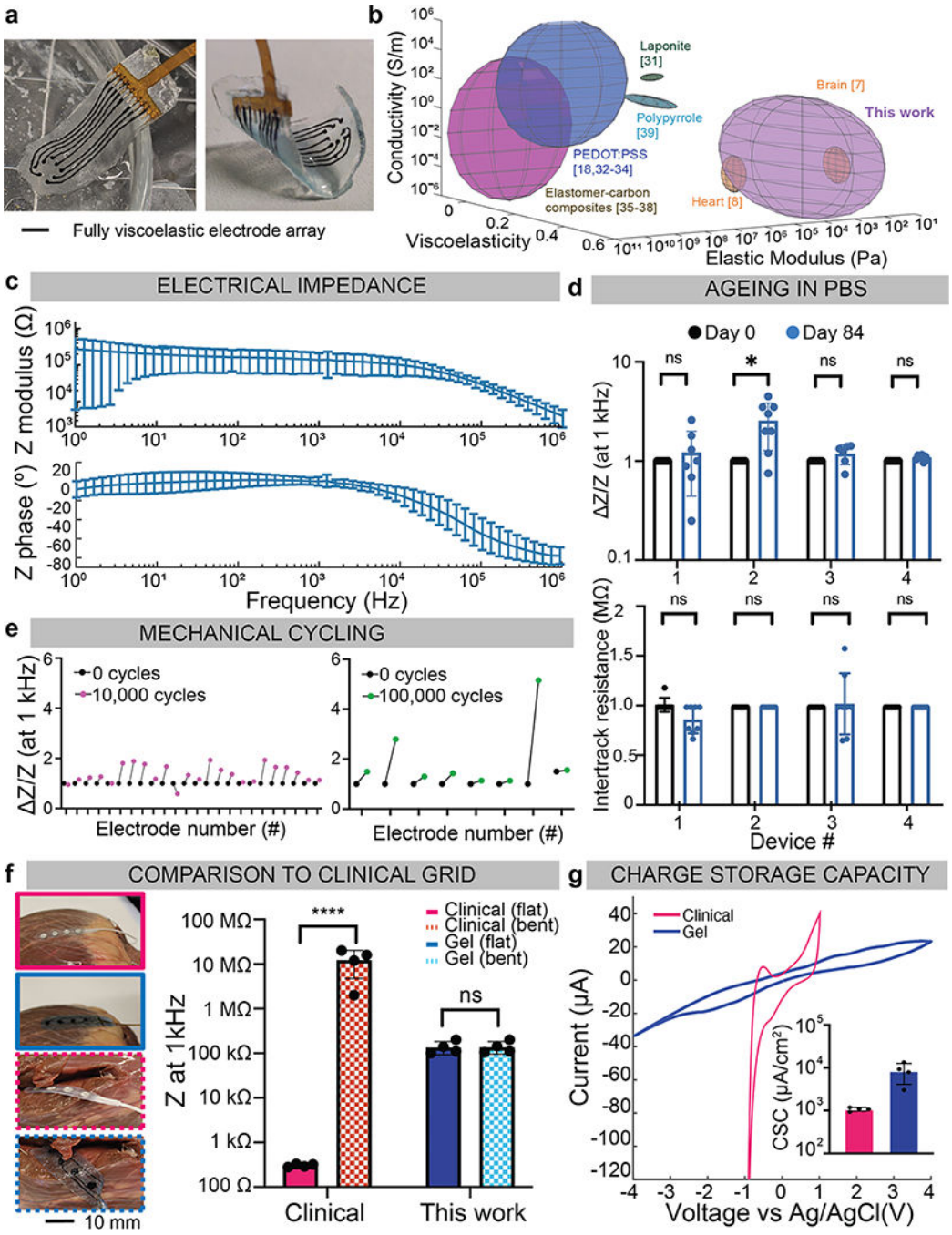

Figure 5: Device characterization and in vitro validation of the fully viscoelastic device.

(a) Photographs of the fully assembled array, 6 mm × 20 mm × 250 μm, with 8 electrodes of d=700 μm and a 1.5 mm pitch, flat in PBS (left), and bent (right). Scale bar represents 3 mm. (b) Quantification of the elastic modulus (Pascals), conductivity (S/m), and viscoelasticity (tan(δ)), of various tissues and conductive composites. Rat heart and brain tissue in orange, represent the targeted physiologic stiffness and viscoelasticity. The alginate-based conductors fabricated in this study are shown in purple. Values for other conductive composites reported in the literature are also represented, using the reported ranges for

each variable. Citations are provided for the values in the illustration, which are taken from the literature in Supplementary Table 2.

(c) Electrical impedance spectroscopy (EIS) data of five devices, from five distinct batches, measured in PBS showing the impedance modulus (left) and impedance phase (right) over a frequency sweep from 1 MHz to 1 Hz. Mean and s.d. of each device plotted, over n=40 of the electrodes.

(d) Comparison of electrode impedance of 4 arrays at 1 kHz, before and after ageing in PBS for 84 days (top). Impedance for each electrode is normalized to the impedance value before ageing. Intertrack resistance between adjacent electrodes, plotted before and after ageing in PBS (bottom), for n=4 independent devices. Numerical data presented as mean ± s.d. (one-way ANOVA and Tukey's HSD post hoc test, *$p<0.05$ ($p=0.02$) and non-significant, n.s., $p>0.05$.

(e) Multiaxial mechanical cycling of viscoelastic arrays, at an equivalent 11% biaxial strain, with the relative change in impedance (DZ/Z) at 1 kHz plotted for each electrode. Three devices were cycled 10,000 times (left, pink) and one device was cycled 100,000 times (right, green).

(f) Photographs of a commercial clinical grid (pink) with a similar-dimensioned viscoelastic array (blue), on a bovine heart (left). Scale bar represents 10 mm. The grids were placed on smooth regions of the tissue (solid line) and bent 90° around the heart (dashed lines). Impedance at 1 kHz is extracted for each electrode (n=4/device) and compared for the flat and bent configurations (right). Mean and s.d. are plotted, with ****$p<0.0001$ and non-significant, n.s., $p>0.05$.

(g) Cyclic voltammetry of an electrode from the commercial grid (pink), and from the viscoelastic array described in this work (blue). Inset bar graph shows the charge storage capacity (CSC) extracted from each electrode (n=4/device) and compared over the four electrodes from each array (inset). Mean and s.d. of each electrode plotted.

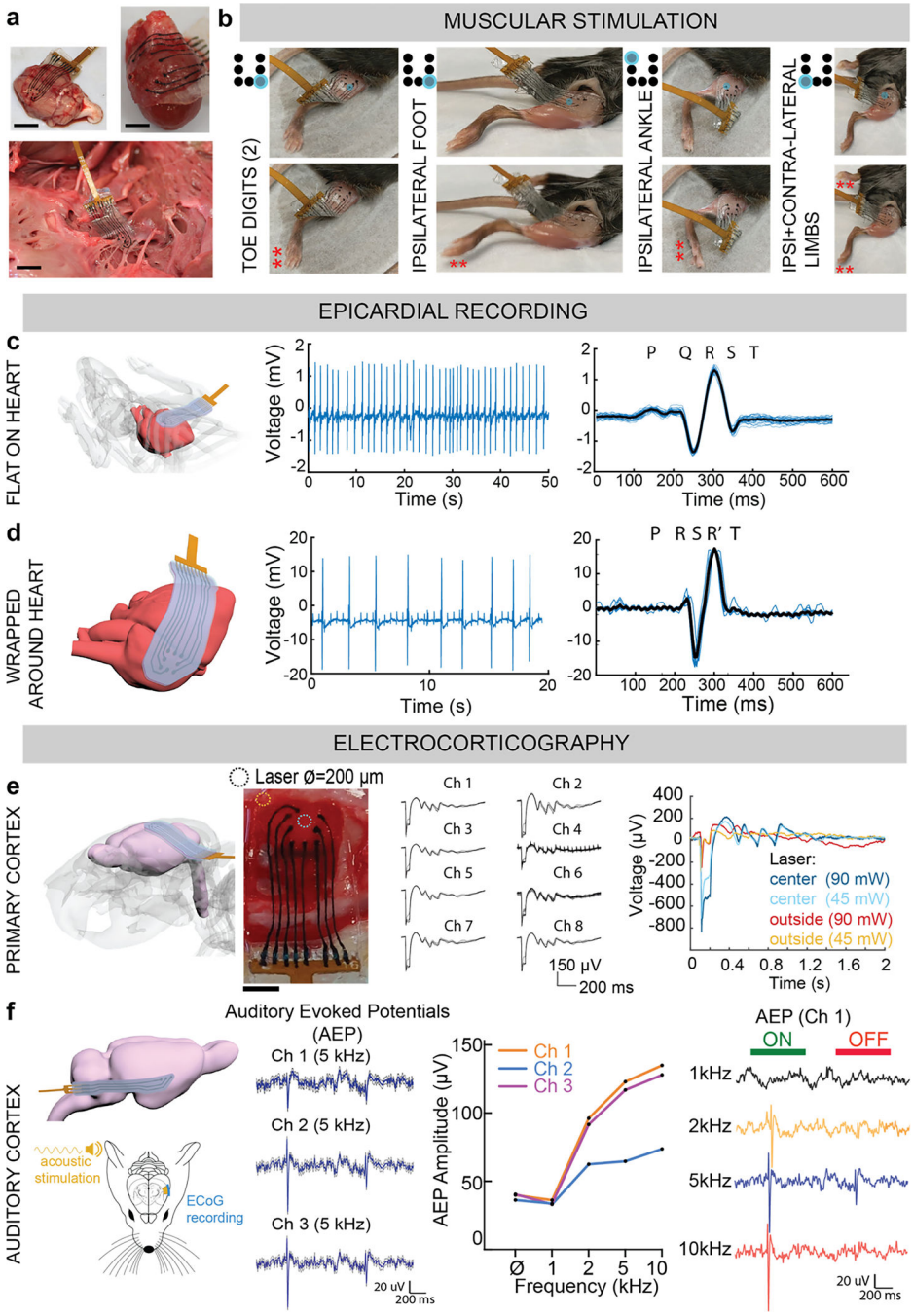

Figure 6: *In vivo* validation of the fully viscoelastic device for stimulation and for recording, even under extreme deformation.

(a) Photographs of the assembled viscoelastic array on a rat cortical surface (top, left), conformed around a rat heart (top, right), and wrapped around the nerves of a bovine heart (bottom). Scale bar: 3 mm.

(b) Photographs, taken from videos, of the viscoelastic array stimulating the exposed muscle of a mouse hindlimb. By positioning the array or changing the electrode applying the stimulation pulses, the toes only (far left), the foot only (left), the ankle (right), or both the contralateral and ipsilateral limbs (far right) are triggered. Red asterisks (**) mark the

portion of the limb responding to stimulation. Schematic to the left of each image shows the representative electrode (blue) that is stimulating the tissue.

(c) Schematic of the viscoelastic array, flat and conformed to the surface of a mouse heart (left). Acute electrical activity recorded *in vivo* from the mouse heart with three electrodes, with the filtered electrocardiogram (EKG) (middle), and superimposed average (black) of all the beats (right). Individual cycles are shown in light blue.

(d) Schematic of the viscoelastic array, wrapped almost 360° around the surface of a mouse heart (left), and remaining conformed. Acute electrical activity recorded *in vivo* from the mouse heart with three electrodes, with the filtered electrocardiogram (EKG) (middle), and superimposed average (black) of all the beats (right). Individual cycles are shown in light blue.

(e) Schematic of the viscoelastic array, placed on the cortical surface of a rat brain (far left). Photograph of the viscoelastic array on top of the exposed dura of a Thy1 rat cortex (left, scale bar: 4 mm), with added circles to show where stimulation from a laser was applied (either at the blue circle: centre of device, or brown circle: lateral edge of device). Acute electrical activity recorded *in vivo*, epidurally from the cortical surface after stimulation by blue light laser, at centre or lateral edge of array. Each electrode depolarization is shown by each respective electrode tracing, as the average and standard deviation over the recording session (top, right). Comparison of the electrical activity recorded by a single channel (Ch) as the laser position changed from the centre of the device (blue curves) to the lateral edge, and as the laser power changed from 90 mW (dark blue and brown traces) to 45 mW (light blue and brown traces).

(f) Schematic of the viscoelastic array, bent more than 90° to reach the auditory cortex of a rat brain (top, left). Schematic of the set-up for recording from the auditory cortex (bottom, left). Acute electrical activity recorded *in vivo*, epidurally from the auditory cortical surface from each of the 3 electrodes (channels) of the array, when an acoustic tone of 5 kHz was applied. In addition to recording auditory evoked potentials (AEP) from each Ch, an independent frequency tuning profile of each Ch was obtained. Tone burst stimulation (duration of 1 second) applied, and AEP recorded from Ch 1, over 4 applied acoustic tones (1, 2, 5, 10 kHz). ‘ON’ (green) and ‘OFF’ (red) of the tone burst are indicated above AEP.